Accurate and fast simulation of remote sensing images at top of atmosphere with DART-Lux

Yingjie Wang, Jean-Philippe Gastellu-Etchegorry

Accurate and fast simulation of remote sensing images at top of atmosphere with DART-Lux

Yingjie WANG[1], Jean-Philippe Gastellu-Etchegorry[1]

[1] CESBIO, CNES-CNRS-IRD-UPS, University of Toulouse, 31401 Toulouse CEDEX 09, France

Correspondence to: Yingjie WANG (yingjiewang1102@gmail.com)

Abstract

DART model is one of the most comprehensive and accurate radiative transfer (RT) models to simulate remotely sensed signals in the Earth-atmosphere system. Its standard RT modelling mode, called DART-FT, relies on the discrete ordinates method. Its recently developed Monte Carlo mode using an unbiased bidirectional path tracing method, called DART-Lux, increases hundredfold DART efficiency to simulate images. Since DART-Lux does not simulate yet atmospheric RT, a hybrid method has been designed to accurately and fast simulate remote sensing images at top of atmosphere (TOA). It couples the atmospheric RT modelling of DART-FT with the very efficient Earth surface RT modelling of DART-Lux. For that, a new sky light modelling, an innovative BRF camera modelling and an adapted radiative coupling framework have been designed. The efficiency and accuracy of this hybrid method have been validated using DART-FT as a reference. Here, we present this validation for a realistic forest stand. Simulation time is reduced by a factor of 750 with a relative difference of solar plane

reflectance factor smaller than 1%. This hybrid method opens new perspectives for the use of 3D modelling in remote sensing applications. It is already part of the DART version freely available for scientists (https://dart.omp.eu).

Key words

DART, Monte Carlo, Top of atmosphere, Radiative transfer, Image simulation

1 Introduction

Remotely sensed images at the top of atmosphere (TOA) are inevitably contaminated by the atmosphere due to scattering, absorption and emission of atmospheric constituents (*e.g.*, gases, aerosols) (Dave, 1980; Myneni and Asrar, 1994; Song et al., 2001; Ueno and Mukai, 1977). Many approaches have been developed to remove or reduce atmospheric effects in TOA images, including empirical methods such as the line method and darkest pixel method (Chavez Jr, 1988; Conel et al., 1987; Crippen, 1987), radiative transfer (RT) modelling methods based on the physics of ray-matter interactions such as 6S (Vermote et al., 1997) and MODTRAN (Berk et al., 1987), and hybrid methods that combine empirical and RT modelling methods (Goetz et al., 1997).

In the absence of field data, modelling TOA radiance is of great interest to better understand radiation interactions in the Earth system and also to better use the remote sensing observations of the Earth surface (Gastellu-Etchegorry et al., 1996; Guanter et al., 2009; Kraska, 1996; Richtsmeier et al., 2001; White et al., 2004; Zahidi, 2019), because it takes into account the physical mechanisms in the coupled Earth-atmosphere system and the instrumental

characteristics that give rise to these TOA images. Most atmospheric RT models (*e.g.*, MODTRAN, 6S) used for atmospheric correction of remote sensing images simulate TOA radiance depending on a-priori knowledge of the Earth surface reflectance anisotropy. For that, they are usually coupled with Earth surface RT models such as DART and SAIL (Verhoef, 1984). However, this coupling approach is usually approximate since it simplifies the 3D nature and topography of the Earth surface as a horizontal plane. In addition, most Earth surface RT models consider that downward atmospheric diffuse radiation is isotropic, which can be a large source of inaccuracy. DART does not make these simplifications because it simulates the Earth-Atmosphere radiative coupling with a 3D approach. It explains that it simulates high accuracy remote sensing images and it is efficient for remote sensing applications.

Based on its discrete ordinates method, called DART-FT, DART is able to simulate remote sensing images of arbitrary 3D urban and natural landscapes with atmosphere. Recently, DART efficiency to simulate BOA remote sensing images of large and complex landscapes has been greatly improved thanks to its newly developed Monte Carlo mode, called DART-Lux (Wang et al., 2021b). DART-Lux uses an unbiased and fast bidirectional path tracing method that improves DART efficiency by a hundredfold in terms of computer time and memory. However, it has not yet been adapted to simulate TOA images. This is due to two major difficulties: (1) Monte Carlo method needs a huge amount of samples to simulate accurate TOA spectrum; (2) Monte Carlo method can cause distortion of TOA spectrum, since all bands share a common path from source to detector while spectral properties usually lead to different path per band (Emde et al., 2011). On the other hand, DART-FT solves the radiative transfer equation per band with the discrete ordinates method (Grau and Gastellu-Etchegorry, 2013). Although the discrete ordinates method is less accurate than the exact monochromatic Monte Carlo method

due to its discretization approximation, it is much more efficient and does not cause distortion issues.

This paper presents a hybrid method that allows DART-Lux to simulate accurate and fast TOA images. It includes a new Monte Carlo modelling of sky lighting, an innovative BRF camera and a coupling framework for Monte Carlo Earth surface RT modelling and non-Monte Carlo atmospheric RT modelling. Its efficiency and accuracy are illustrated with a simulation of a realistic forest stand. The relationship between accuracy and simulation time is also discussed.

2 Background and method

DART is developed at CESBIO since 1992 (Figure 1). It is one of the most comprehensive and accurate 3D RT models in the optical remote sensing community (Gastellu-Etchegorry et al., 2017, 1996). It has been successfully validated against field measurements and through RAdiation Model Intercomparison (RAMI) (Grau and Gastellu-Etchegorry, 2013; Guillevic et al., 2003, 2013; Pinty et al., 2004, 2001; Wang and Gastellu-Etchegorry, 2020; Widlowski et al., 2015, 2013, 2007). Its standard mode, called DART-FT, simulates the bidirectional reflectance factor (BRF), directional brightness temperature (DBT) and remote sensing images of arbitrary 3D natural and urban landscapes, with topography and atmosphere, from visible to thermal infrared domain. Its newly developed Monte Carlo mode, called DART-Lux, increases hundredfold efficiency to simulate the RT in Earth surface. DART-Lux accuracy for simulating BOA images, fluorescence and LiDAR signals has already been validated by DART-FT.

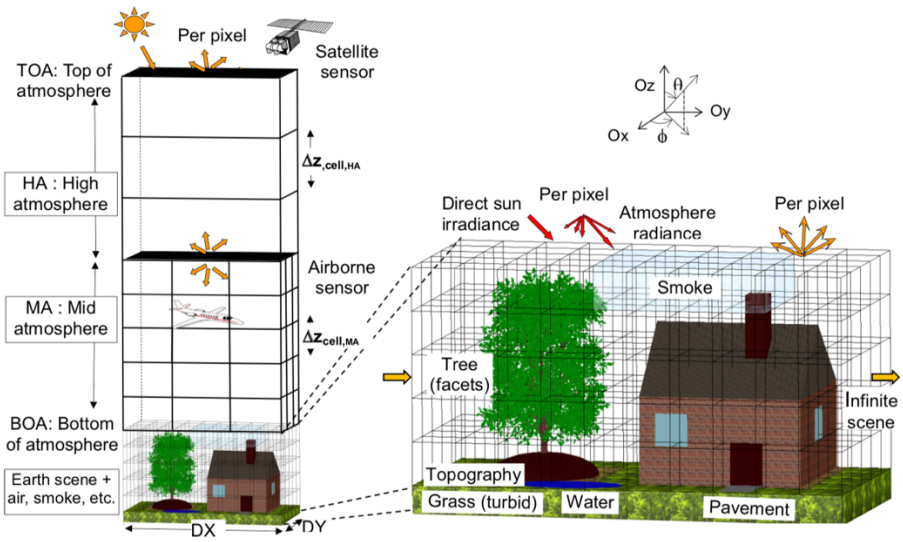

Figure 1. DART-FT 3D discrete mock-up. Landscape elements are made of triangles, and/or fluid and turbid medium in a cell array. In DART-Lux, the simulation of landscapes is similar to that of DART-FT without using a cell array.

2.1 Earth-atmosphere radiative coupling

DART-FT simulates sequentially the atmospheric RT and Earth surface RT and couples them. Its RT modelling relies on the discrete ordinates method that iteratively tracks rays along finite discrete directions. Figure 2 illustrates the 5 major steps of DART RT modelling in the coupled Earth-atmosphere system in order to simulate TOA images (Grau and Gastellu-Etchegorry, 2013; Wang et al., 2020):

(1) Sun illumination followed by atmosphere scattering and thermal emission.

(2) Earth surface RT.

(3) Earth-atmosphere radiative coupling.

(4) Earth surface RT of atmosphere backscattered radiation.

(5) Transfer of BOA upward radiation to TOA.

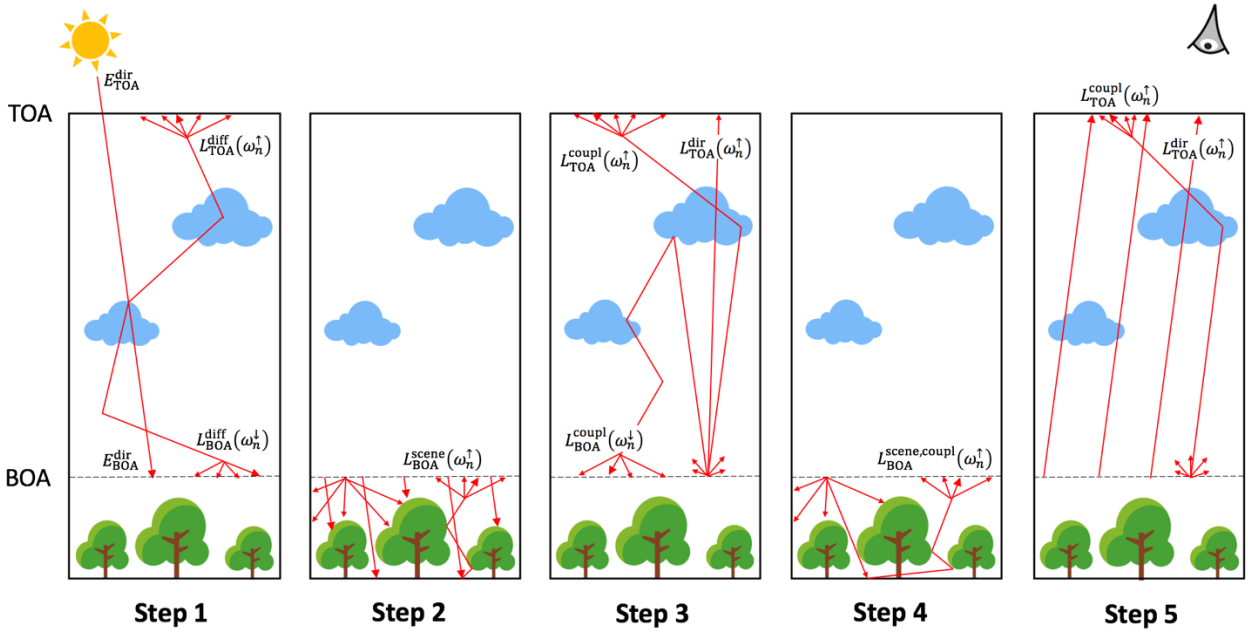

Figure 2. Major steps to model RT in the Earth-atmosphere system. Step 1: Sun illumination, thermal emission and atmosphere scattering. Step 2: Earth surface RT, including scene scattering and emission. Step 3: Earth-atmosphere radiative coupling. Step 4: Earth surface RT of atmosphere backscattered radiation. Step 5: Transfer of BOA upward radiation to TOA.

2.2 Hybrid method for simulating TOA images

DART-Lux models the Earth surface RT using the Monte Carlo based bidirectional path tracing method (Veach, 1997; Veach and Guibas, 1995a, 1995b). This method simulates the remote sensing signals by sampling a group of paths between the light source and the detector and evaluates the contribution of these path samples. It can increase DART efficiency by a hundredfold to simulate remote sensing images of complex 3D landscapes (Wang et al., 2021b). However, this new Monte Carlo modelling is not yet adapted to simulate the atmospheric RT. Since DART-FT simulates efficiently the atmospheric RT, a hybrid method is proposed to simulate TOA images that takes advantage of fast DART-Lux Earth surfaces RT modelling and fast DART-FT atmospheric RT modelling.

The three following sections present the details of the hybrid method:

- A new Monte Carlo modelling of the anisotropic sky lighting.
- An innovative BRF camera modelling to capture directional radiation exiting the Earth surface.
- A framework to couple Monte Carlo Earth surface RT and non-Monte Carlo Atmospheric RT.

2.2.1 Anisotropic sky lighting

Figure 3 illustrates the sky lighting. The Monte Carlo method models the sky lighting by sampling a random direction ω_0 and a start vertex p_0 on the virtual disk that is the projection of the scene sphere along ω_0 (Figure 3). Most Monte Carlo RT models consider sky light to be isotropic (e.g., (Qi et al., 2019)) or compute the sky light with empirical equations (e.g., (Pharr et al., 2016)). With the aim of better precision, we designed a new method to accurately model the anisotropic sky light. This method uses the DART-FT computed BOA diffuse radiance. Note that it can use BOA diffuse radiance computed by other atmospheric RT models.

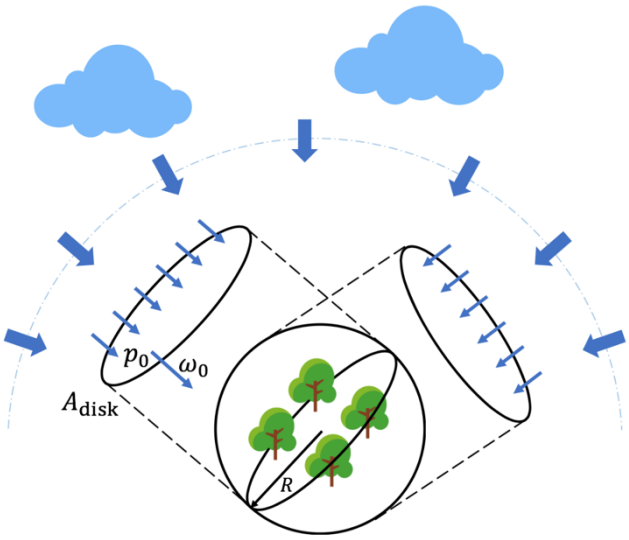

Figure 3. Sky lighting. The Earth scene is in a sphere of radius R. It is illuminated by the light from the sky dome.

DART-FT tracks radiations along N_Ω predefined discrete directions $\omega_n(\Delta\omega_n)$ with $n \in [1, N_\Omega]$ (Yin et al., 2013). The computed sky light is stored per discrete downward direction per band $L_{\mathrm{BOA}}^{\mathrm{diff}}(\omega_n^{\downarrow}, \lambda)$. In order to adapt to Monte Carlo method such as DART-Lux that samples arbitrary sky light direction, we designed a 2D distribution sampler. We first resample $L_{\mathrm{BOA}}^{\mathrm{diff}}(\omega_n^{\downarrow}, \lambda)$ from discrete directions to directions with equal angle step (angle steps $\Delta\theta$ and $\Delta\varphi$, angle numbers: $N_\theta = \frac{\pi/2}{\Delta\theta}$ and $N_\varphi = \frac{2\pi}{\Delta\varphi}$) (Figure 4). It results that pixel (*i*, *j*) on the hemisphere stores $L(\omega_{i,j}, \lambda) = L_{\mathrm{BOA}}^{\mathrm{diff}}(\omega_n^{\downarrow}, \lambda)$ if $\omega_{i,j} \in \Delta\omega_n$. Below, the wavelength term λ is omitted for compactness.

Then, a direction is sampled with the probability density function (PDF) $p(\omega) = \frac{p(\theta,\varphi)}{\sin\theta}$ where $p(\theta, \varphi)$ is constructed by Eq. (1). $p(\theta, \varphi)$ and radiance $\bar{L}(\omega_{i,j})$ are constant in $\Delta\omega_{i,j}$. $\bar{L}(\omega_{i,j})$ is the mean radiance of all spectral bands along $\omega_{i,j}$. It is only used to compute the PDF.

$$p(\theta,\varphi) = \frac{\int_{\Delta\omega_{i,j}} \bar{L}(\omega)\cdot\cos\theta\cdot\sin\theta\cdot d\theta\cdot d\varphi/(\Delta\theta\cdot\Delta\varphi)}{\int_{2\pi}\int_{\pi/2} \bar{L}(\omega)\cdot\cos\theta\cdot\sin\theta\cdot d\theta\cdot d\varphi} = \frac{\bar{L}(\omega_{i,j})\cdot\sin(2\theta_i)\cdot\frac{\sin\Delta\theta}{\Delta\theta}}{\sum_{i'=1}^{N_\theta}\sum_{j'=1}^{N_\varphi}\bar{L}(\omega_{i',j'})\cdot\sin(2\theta_{i'})\cdot\sin\Delta\theta\cdot\Delta\varphi} \quad (1)$$

with

$$\begin{cases} p(\theta) = \int_{2\pi} p(\theta,\varphi)d\varphi = \sum_{j=1}^{N_\varphi} p(\theta,\varphi)\cdot\Delta\varphi \\ p(\varphi|\theta) = \dfrac{p(\theta,\varphi)}{p(\theta)} \end{cases} \quad (2)$$

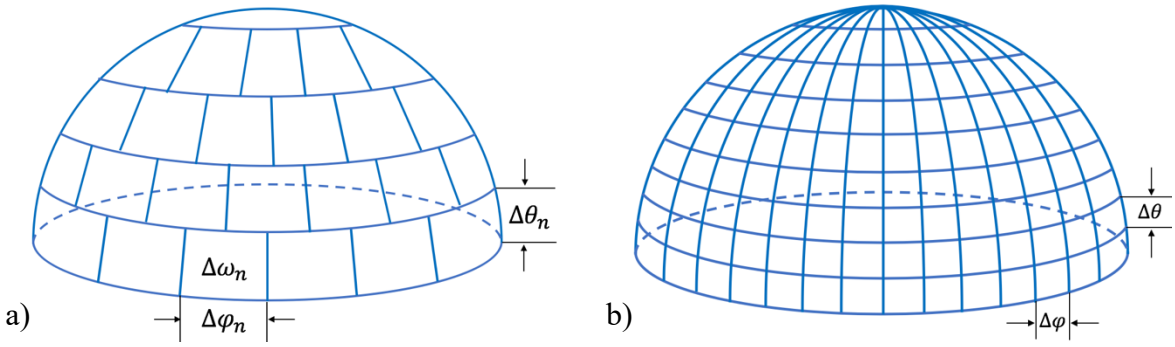

Figure 4. Radiance resampling from discrete directions to equal angle step directions. a) DART-FT discrete directions with solid angle $\Delta\omega_n$ ($\Delta\theta_n$, $\Delta\varphi_n$). b) Resampled equal angle step directions on the hemisphere with constant $\Delta\theta$ and $\Delta\varphi$ for each solid angle.

2.2.2 BRF camera and anisotropic upward fluxes

To couple Earth surface RT with atmospheric RT, one must compute the anisotropic upward radiance from the Earth surface. Most Monte Carlo models compute the directional fluxes by repeatedly simulating directional images, which is very inefficient. In order to avoid this inefficient approach, we designed and implemented an innovative "BRF camera" in DART-Lux. This BRF camera simulates directional upward fluxes in a single run. It has infinite radius to capture the upward radiance from the Earth scene. The conceptional hemispherical sensor is shown in Figure 5.b. It has $N_\theta \cdot N_\varphi$ pixels, with $N_\theta = \frac{\pi/2}{\Delta\theta}$ and $N_\varphi = \frac{2\pi}{\Delta\varphi}$. $\Delta\theta$ and $\Delta\varphi$ are respectively the step of zenith and azimuth angles. It corresponds to $N_\theta \cdot N_\varphi$ orthographic cameras (Figure 5.a) placed around the 3D scene. The average radiance captured by each orthographic camera is stored in the corresponding pixel.

This BRF camera modelling was adapted to the Monte Carlo models of interest (i.e., backward, forward, bi-directional path tracing). For that, a viewing direction is sampled with directional

PDF $p(\omega_0)$ (Eq. (3)) and a depart point is uniformly sampled on the scene ortho-projected surface $A_{\text{ortho}}(\omega_0)$ along the viewing direction ω_0.

$$p(\omega_0) = \frac{p(\theta,\varphi)}{\sin\theta}, \text{with} \begin{cases} p(\theta) = \dfrac{1}{\pi/2} \\ p(\varphi|\theta) = \dfrac{1}{2\pi} \end{cases} \quad (3)$$

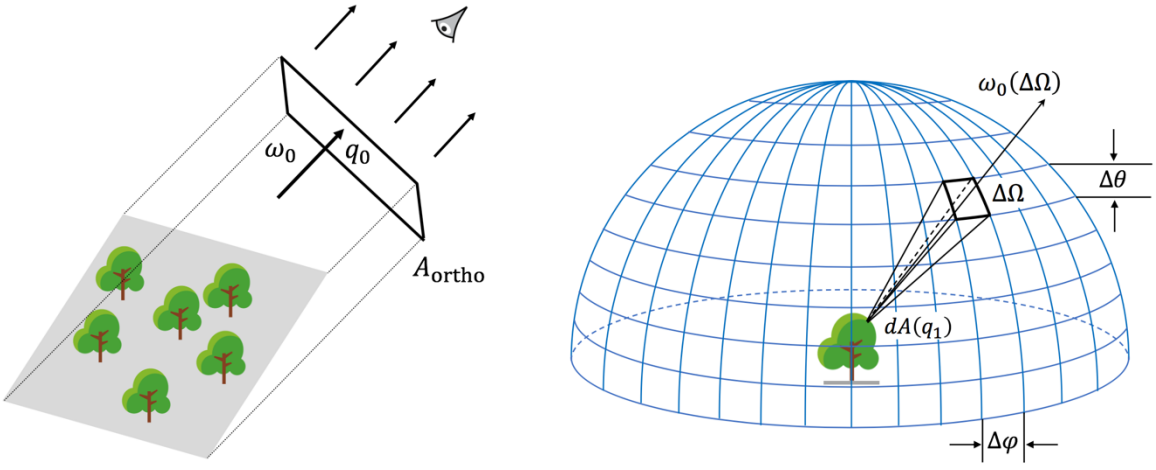

a) b)

Figure 5. a) Radiation exits the Earth scene along direction ω_0 reaches a virtual orthographic plane $A_{\text{ortho}}(\omega_0)$ (detector) that is the projection of the scene along the viewing direction ω_0. b) BRF camera. The hemispheric sensor of the camera has infinite radius from the Earth scene. Any radiation along viewing direction $\omega_0(\Delta\Omega)$ is captured by a pixel on the hemisphere.

After the Earth surface RT modelling, the image of BRF camera that maps the upward directional radiance is created (Figure 6). In a latter step, this radiance map is used to compute the radiance and BRF for any viewing direction. Pixel (i, j) gives the radiance $L(\omega_{i,j})$ for

direction $\omega_{i,j}$ on the hemisphere (Figure 4.b), which allows one to compute the upward radiance $L_{\mathrm{BOA}}^{\mathrm{scene}}\left(\omega_n^{\uparrow}\right)$ along any discrete direction ω_n:

$$L_{\mathrm{BOA}}^{\mathrm{scene}}\left(\omega_n^{\uparrow}\right) = \frac{\int_{\Delta\omega_n} L(\omega)\cdot\cos\theta\cdot\sin\theta\, d\theta d\varphi}{\int_{\Delta\omega_n}\cos\theta\cdot\sin\theta\, d\theta d\varphi} = \frac{\sum_{i=i_0}^{i_1}\sum_{j=j_0}^{j_1} L\left(\omega_{i,j}\right)\cdot\sin(2\theta_i)\cdot\sin\Delta\theta\cdot\Delta\varphi}{\cos\theta_n^c\cdot\Delta\omega_n} \quad (4)$$

where solid angle $\Delta\omega_n$ covers pixel region from line i_0 to i_1 and from column j_0 to j_1. The effective zenith angle θ_n^c of direction ω_n verifies: $\cos\theta_n^c \cdot \Delta\omega_n = \int_{\Delta\omega_n}\cos\theta\cdot\sin\theta\, d\theta d\varphi$.

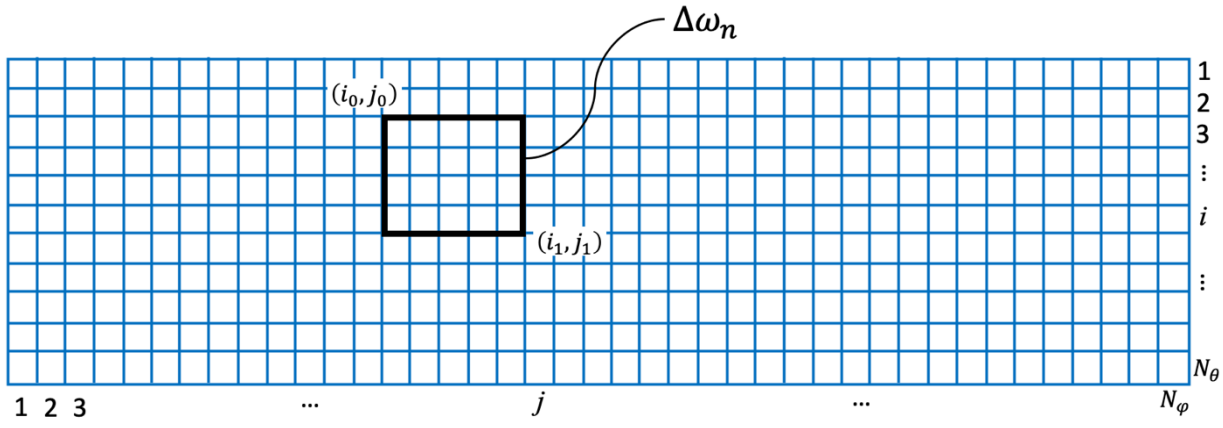

Figure 6. Radiance map simulated by the BRF camera. It has N_θ lines and N_φ columns. The value of pixel (i, j) is the scene radiance along direction $\omega_{i,j}$. The black rectangle outlines the region of a solid angle $\Delta\omega_n$ of discrete direction ω_n. θ_i and φ_j represent the zenith and azimuth angle at centre of pixel (i, j) respectively.

2.2.3 Radiative coupling framework

In the hybrid method, the DART-FT atmospheric RT modelling realizes the steps 1, 3 and 5 of the five major radiative steps (Figure 2), while the DART-Lux Earth surface RT modelling

realizes steps 2 and 4, plus an additional step 6. Steps 1 to 5 give spatially averaged radiance values conversely to step 6 that gives images. These steps are detailed below.

1) DART-FT atmospheric RT modelling. TOA direct irradiance $E_{\mathrm{TOA}}^{\mathrm{dir}}$ leads to diffuse radiance $L_{\mathrm{TOA}}^{\mathrm{diff}}\left(\omega_n^{\uparrow}\right)$ per upward direction $\omega_n^{\uparrow}$, BOA direct irradiance $E_{\mathrm{BOA}}^{\mathrm{dir}}$, BOA diffuse irradiance $E_{\mathrm{BOA}}^{\mathrm{diff}}$ and BOA diffuse radiance $L_{\mathrm{BOA}}^{\mathrm{diff}}\left(\omega_n^{\downarrow}\right)$ per downward direction $\omega_n^{\downarrow}$.

2) DART-Lux Earth surface RT modelling. It uses two light sources: sunlight with direct irradiance $E_{\mathrm{BOA}}^{\mathrm{dir}}$ and anisotropic sky light with BOA diffuse radiance $L_{\mathrm{BOA}}^{\mathrm{diff}}\left(\omega_n^{\downarrow}\right)$. This step gives the upward scene radiance $L_{\mathrm{BOA}}^{\mathrm{scene}}\left(\omega_n^{\uparrow}\right)$ per upward direction $\omega_n^{\uparrow}$ using Eq. (4).

3) DART-FT atmospheric RT modelling. It computes the transfer functions $\mathrm{TF}_{\mathrm{BA-BA}}$ (*i.e.*, BOA downward radiance $L_{\mathrm{BOA}}^{\mathrm{coupl}}\left(\omega_n^{\downarrow}\right)$ contributed by BOA upward radiance $L_{\mathrm{BOA}}^{\mathrm{scene}}(\omega_n^{\uparrow})$) and $\mathrm{TF}_{\mathrm{BA-TOA}}$ (*i.e.*, TOA radiance $L_{\mathrm{TOA}}^{\mathrm{coupl}}\left(\omega_n^{\uparrow}\right)$ contributed by BOA upward radiance $L_{\mathrm{BOA}}^{\mathrm{scene}}(\omega_n^{\uparrow})$). Then, $L_{\mathrm{BOA}}^{\mathrm{coupl}}\left(\omega_n^{\downarrow}\right)$ is extrapolated to infinite coupling order radiance $L_{\mathrm{BOA}}^{\mathrm{coupl}(\infty)}\left(\omega_n^{\downarrow}\right)$ using the Earth scene albedo ρ and atmosphere backscattering albedo s (Eq. (5)). The backscattered irradiance $E_{\mathrm{BOA}}^{\mathrm{coupl}(\infty)}$ is computed using $L_{\mathrm{BOA}}^{\mathrm{coupl}(\infty)}\left(\omega_n^{\downarrow}\right)$:

$$
\begin{aligned}
L_{\mathrm{BOA}}^{\mathrm{coupl}(\infty)}\left(\omega_n^{\downarrow}\right) &= \frac{1}{1-\rho\cdot s}\cdot L_{\mathrm{BOA}}^{\mathrm{coupl}}\left(\omega_n^{\downarrow}\right) \\
E_{\mathrm{BOA}}^{\mathrm{coupl}(\infty)} &= \sum\nolimits_{\omega_n^{\downarrow}} L_{\mathrm{BOA}}^{\mathrm{coupl}(\infty)}\left(\omega_n^{\downarrow}\right)\cdot\cos\theta_n^{c}\cdot\Delta\omega_n
\end{aligned}
\tag{5}
$$

with

$$\rho = \frac{\sum_{\omega_n^{\uparrow}} L_{\mathrm{BOA}}^{\mathrm{scene}}\left(\omega_n^{\uparrow}\right) \cdot \cos\theta_n^c \cdot \Delta\omega_n}{E_{\mathrm{BOA}}^{\mathrm{dir}} + E_{\mathrm{BOA}}^{\mathrm{diff}}}$$

$$s = \frac{\sum_{\omega_n^{\downarrow}} L_{\mathrm{BOA}}^{\mathrm{coupl}}\left(\omega_n^{\downarrow}\right) \cdot \cos\theta_n^c \cdot \Delta\omega_n}{\sum_{\omega_n^{\uparrow}} L_{\mathrm{BOA}}^{\mathrm{scene}}\left(\omega_n^{\uparrow}\right) \cdot \cos\theta_n^c \cdot \Delta\omega_n} \tag{6}$$

4) DART-Lux surface RT modelling. It uses a single light source: the extrapolated anisotropic sky light with radiance $L_{\mathrm{BOA}}^{\mathrm{coupl}(\infty)}\left(\omega_n^{\downarrow}\right)$. It computes the scene radiance per upward direction $\omega_n^{\uparrow}$ using Eq. (4), which added to $L_{\mathrm{BOA}}^{\mathrm{scene}}\left(\omega_n^{\uparrow}\right)$ gives $L_{\mathrm{BOA}}^{\mathrm{scene,coupl}}\left(\omega_n^{\uparrow}\right)$.

5) $\mathrm{TF}_{\mathrm{BA-TOA}}$ is applied to compute direct transmitted radiance $L_{\mathrm{TOA}}^{\mathrm{dir}}\left(\omega_n^{\uparrow}\right)$ and scattered radiance $L_{\mathrm{TOA}}^{\mathrm{coupl}}\left(\omega_n^{\uparrow}\right)$ per upward direction using $L_{\mathrm{BOA}}^{\mathrm{scene,coupl}}\left(\omega_n^{\uparrow}\right)$.

6) DART-Lux Earth surface RT modelling. It uses two light sources: sunlight with irradiance $E_{\mathrm{BOA}}^{\mathrm{dir}}$ and anisotropic sky light with BOA diffuse radiance $L_{\mathrm{BOA}}^{\mathrm{diff}}(\omega_n^{\downarrow}) + L_{\mathrm{BOA}}^{\mathrm{coupl}(\infty)}(\omega_n^{\downarrow})$. It gives BOA upward radiance images $L_{\mathrm{BOA}}\left(i,j,\omega_n^{\uparrow}\right)$. TOA radiance images are computed as:

$$L_{\mathrm{TOA}}\left(i,j,\omega_n^{\uparrow}\right) = L_{\mathrm{BOA}}\left(i,j,\omega_n^{\uparrow}\right) \cdot \frac{L_{\mathrm{TOA}}^{\mathrm{dir}}\left(\omega_n^{\uparrow}\right)}{L_{\mathrm{BOA}}^{\mathrm{scene,coupl}}\left(\omega_n^{\uparrow}\right)} + L_{\mathrm{TOA}}^{\mathrm{diff}}\left(\omega_n^{\uparrow}\right) + L_{\mathrm{TOA}}^{\mathrm{coupl}}\left(\omega_n^{\uparrow}\right) \tag{7}$$

Reflectance images can be also computed:

$$\rho_{\mathrm{BOA}}\left(i,j,\omega_n^{\uparrow}\right) = \frac{L_{\mathrm{BOA}}\left(i,j,\omega_n^{\uparrow}\right)}{E_{\mathrm{BOA}}^{\mathrm{dir}} + E_{\mathrm{BOA}}^{\mathrm{diff}} + E_{\mathrm{BOA}}^{\mathrm{coupl}(\infty)}},\ \rho_{\mathrm{TOA}}\left(i,j,\omega_n^{\uparrow}\right) = \frac{L_{\mathrm{TOA}}\left(i,j,\omega_n^{\uparrow}\right)}{E_{\mathrm{TOA}}^{\mathrm{dir}}} \tag{8}$$

3 Results and discussion

3.1 Validation with realistic forest stand

The accuracy and efficiency of the presented hybrid method (hereinafter, it is referred by DART-Lux) are assessed by comparing its results with those of DART-FT for a 30 m × 30 m plot of Järvselja Birch forest (summer) from RAMI experiment (https://rami-benchmark.jrc.ec.europa.eu; (Widlowski et al., 2015)) (Figure 7). This plot contains 91 trees including 50 birch trees, 18 linden trees, 15 aspen trees, 5 spruce trees, and 3 ash and maple trees (Figure 7). We did not consider the full 100 m × 100 m birch forest that contains more than 550 million of facets because it would have required too much RAM and computation time for DART-FT.

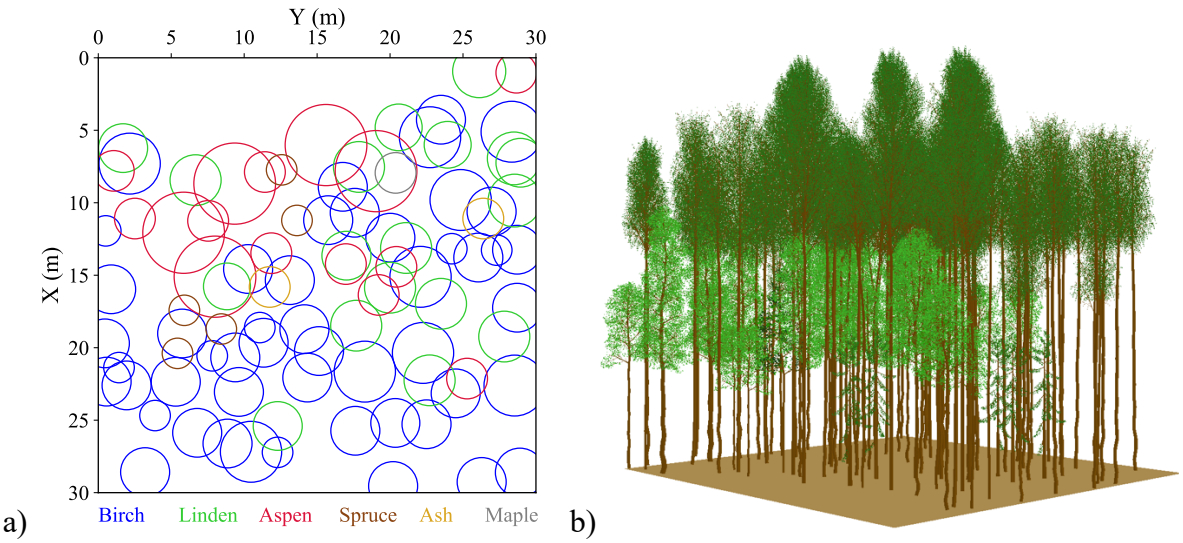

Figure 7. The 30 m × 30 m plot of Järvselja birch forest. a) Spatial distribution of tree species. b) DART 3D mock-up.

Table 1. Optical properties of ground and tree species for four spectral band. ρ is the reflectance and τ is the transmittance.

3D object	Optical properties	B	G	R	NIR
Birch	ρ_{leaf}	0.045	0.104	0.039	0.474
	τ_{leaf}	0.000	0.110	0.012	0.483
	ρ_{branch}	0.072	0.094	0.101	0.464
	ρ_{trunk}	0.355	0.410	0.436	0.539
Linden	ρ_{leaf}	0.045	0.073	0.035	0.442
	τ_{leaf}	0.000	0.074	0.004	0.462
	ρ_{branch}	0.125	0.167	0.206	0.363
	ρ_{trunk}	0.125	0.167	0.206	0.363
Aspen	ρ_{leaf}	0.045	0.078	0.036	0.436
	τ_{leaf}	0.000	0.107	0.009	0.517
	ρ_{branch}	0.111	0.107	0.118	0.266
	ρ_{trunk}	0.169	0.189	0.215	0.441
Spruce	ρ_{leaf}	0.045	0.077	0.036	0.447
	τ_{leaf}	0.000	0.044	0.002	0.369
	ρ_{branch}	0.117	0.141	0.155	0.363
	ρ_{trunk}	0.117	0.141	0.155	0.363
Ash	ρ_{leaf}	0.045	0.098	0.038	0.516
	τ_{leaf}	0.000	0.046	0.002	0.379
	ρ_{branch}	0.125	0.167	0.206	0.363
	ρ_{trunk}	0.125	0.167	0.206	0.363
Maple	ρ_{leaf}	0.046	0.123	0.042	0.465
	τ_{leaf}	0.001	0.155	0.025	0.025

	ρ_{branch}	0.125	0.167	0.206	0.363
	ρ_{trunk}	0.125	0.167	0.206	0.363
Ground	$\rho_{\text{background}}$	0.019	0.058	0.032	0.329

DART-FT and DART-Lux simulations are conducted with direct sun illumination ($\theta_{\text{sun}} = 36.6°, \varphi_{\text{sun}} = 270.69°$), THKUR TOA irradiance spectra (Berk et al., 2008), a 0.125 m spatial resolution and 4 spectral bands (blue: 0.44 μm, green: 0.55 μm, red: 0.66 μm, NIR: 0.87 μm), with 6 scattering orders at most. The atmosphere model is mid-latitude summer (Anderson et al., 1986) and the aerosol model is rural (Shettle and Fenn, 1979). Specific optical properties were assigned per tree species (Table 1). Here, DART-Lux is run with 800 samples per pixel and DART-FT is run with 62500 illumination rays per pixel, and 1000 discrete directions. DART-FT and DART-Lux BOA colour composite images are shown in Figure 8.a, d. The associated scatter plot of BOA pixel reflectance (Figure 9.a) gives R-squared > 0.92 and bias ≈ 0.01. Densities of scatter points are shown by colours in order to stress that most points are on the diagonal. TOA colour composite images are shown in Figure 8.b, e. The associated scatter plot of TOA pixel reflectance (Figure 9.b) gives R-squared ≈ 0.92 and bias ≈ 0.01. Scatter points outside the diagonal are mainly due to DART-Lux Monte Carlo noises and to DART-FT discretization. By averaging the image resolution from 0.125 m to 1.0 m, which more or less compensates these effects, scatter plots become more linear, with R-square > 0.998 and bias ≈ 0.0002 (Figure 9.c). We also assessed the BRF accuracy in the solar plane by computing the average absolute relative "DART-Lux - DART-FT" BRF difference $\bar{\varepsilon}=\frac{1}{N_{\theta_v}}\cdot\sum_{\theta_v}\frac{|\rho_{\text{DART-Lux}}(\theta_v)-\rho_{\text{DART-FT}}(\theta_v)|}{\rho_{\text{DART-FT}}(\theta_v)}\cdot 100\%$ with N_{θ_v} viewing directions in the solar plane with zenith angle step $\Delta\theta_v=2°$. Here, $\bar{\varepsilon}$ is 1.0% at BOA level and 0.8% at TOA level.

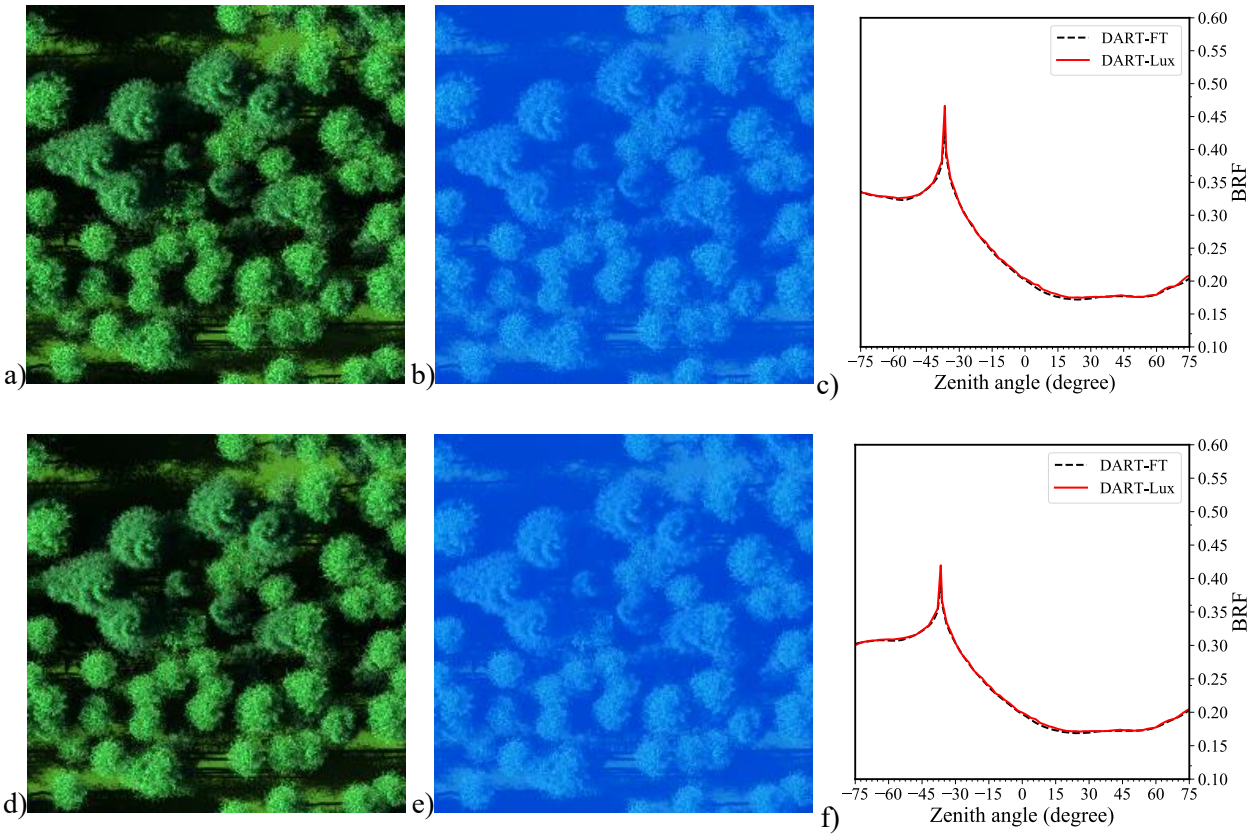

Figure 8. Nadir colour composite images of the forest plot shown in Figure 7. DART-FT BOA (a) and TOA (b) images. DART-Lux BOA (d) and TOA (e) images. DART-FT and DART-Lux BOA (c) and TOA (f) BRFs at NIR band in the solar plane, with 2° zenith angle step.

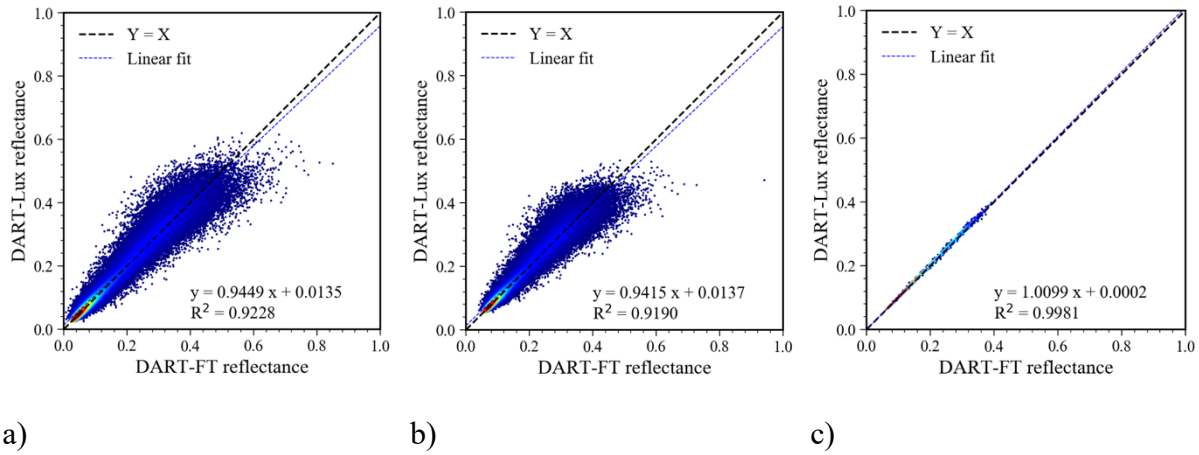

Figure 9. Pixelwise comparison of DART-FT and DART-Lux nadir images at NIR band. a) BOA. 0.125 m resolution. b) TOA. 0.125 m resolution. c) TOA. 1.0 m resolution.

Therefore, DART-Lux and DART-FT give similar results but DART-Lux has two major advantages: much smaller computer time and RAM. In this simulation, DART-FT takes 86.35 hours and 305.5 Gb RAM on a server (Intel Xeon E5-2687W @ 3.1 GHz, 40 cores) for steps 2 and 4 in Figure 2 whereas DART-Lux takes only 2.3 minutes and 1.2 Gb RAM to simulate the spectral nadir image or the spectral radiance map (*i.e.*, steps 2, 4 and 6 take a total of 6.9 minutes). Compared to DART-FT, DART-Lux computer time is reduced by a factor of 750 and the required RAM is reduced by a factor of 255. Since the atmospheric RT modelling for stratified 1D atmosphere in steps 1, 3 and 5 takes much less time than the Earth surface RT modelling in steps 2 and 4, the hybrid method greatly accelerates the simulation of TOA images.

3.2 Discussion

Monte Carlo method is usually the most precise RT method since no approximations are applied. It gives exact results after running a sufficient long time. However, we have to balance the computation time and the accuracy in practical applications. Based on the simulation of the forest stand (Figure 7) in step 2, we did a sensitivity study about the time cost and the accuracy using DART-Lux. The time cost is quantified by the samples/pixel since time increases linearly with this ratio. Accuracy is quantified by two variables: image mean reflectance difference $\varepsilon_{\mathrm{mean}}$ and root-mean-square-error (RMSE) $\varepsilon_{\mathrm{pixel}}$ of all pixel reflectance by comparing with a reference simulation with 2000 samples/pixel. Table 2 summarizes results. It illustrates three major points: 1) $\varepsilon_{\mathrm{mean}}$ and $\varepsilon_{\mathrm{pixel}}$ decrease nearly exponentially with the increase of samples/pixel. 2) The image mean reflectance converges much faster than image pixel reflectance. 3) The low reflectance band (G) converges much faster than high reflectance band (NIR). It indicates that the DART-Lux simulation time can be optimised according to the application and accuracy requirements. For example, with the above-mentioned computer and

configuration and RMSE accuracy 0.05 of the NIR band pixel reflectance, DART-Lux takes 5.25 minutes and 3.3 Gb RAM to simulate nadir BOA and TOA images of the 100 m × 100 m RAMI forest stand (Figure 10).

Table 2. Mean reflectance error $\varepsilon_{\text{mean}}$ and RMSE of image pixel reflectance $\varepsilon_{\text{pixel}}$ for different samples/pixel ratios and for G and NIR bands. The reference image is simulated with 2000 samples/pixel.

	Samples/pixel	**10**	**25**	**50**	**100**	**200**	**400**	**800**
G	$\varepsilon_{\text{mean}}$	5.8e-5	1.2e-5	1.6e-5	1.1e-5	6.1e-6	2.3e-6	4.9e-6
	$\varepsilon_{\text{pixel}}$	0.011	0.007	0.005	0.004	0.003	0.002	0.0015
NIR	$\varepsilon_{\text{mean}}$	1.2e-4	3.5e-4	4.1e-5	4.1e-5	2.4e-5	1.8e-5	5.5e-6
	$\varepsilon_{\text{pixel}}$	0.094	0.061	0.043	0.031	0.022	0.017	0.013

a) 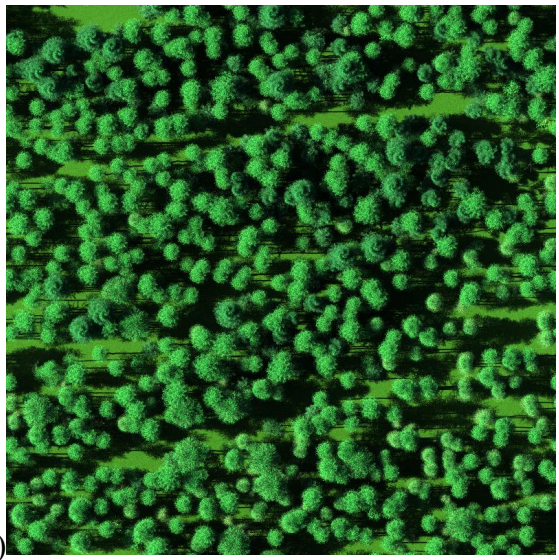 b) 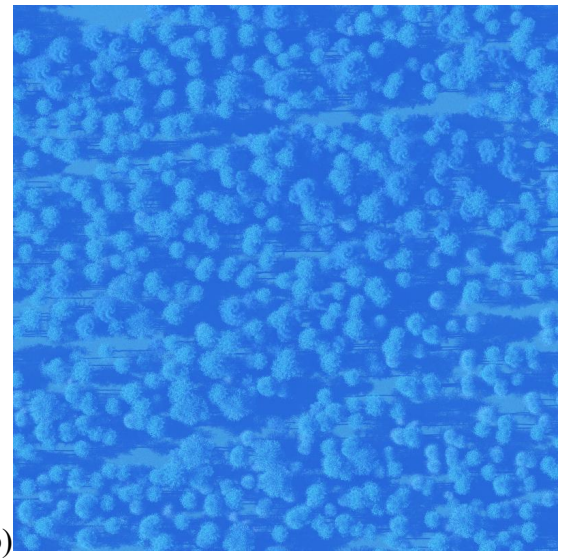

Figure 10. DART-Lux BOA (a) and TOA (b) colour composite nadir images of the 100 m × 100 m Järvselja birch forest stand.

4 Concluding remarks

This paper proposes a new Monte Carlo sky lighting modelling, an innovative BRF camera modelling and a coupling framework in order to (1) couple Monte Carlo Earth surface RT modelling with non-Monte Carlo atmospheric RT modelling and to (2) accurate and fast simulate TOA images. The efficiency of this hybrid method is illustrated here with a realistic forest stand, using DART-FT as a reference. Compared to DART-FT, DART-Lux decreased computer time by a factor of 750 and the need of RAM by a factor of 255. Also, the average absolute relative difference of solar plane BRF profile is 0.8% at TOA. The pixelwise reflectance comparison of TOA image shows good agreement with R-squared ≈ 0.92 and bias ≈ 0.01 at 0.125m resolution, and R-squared > 0.998 and bias ≈ 0.0002 at 1m resolution. A sensitivity study of accuracy in function of simulation time shows that pixel RMSE decreases nearly exponentially with simulation time. It stresses that DART-Lux offers the advantage to set computation time as a function of the expected accuracy. This accurate and fast hybrid method opens new perspectives for DART model applications. Readers are referred to DART user manual (https://dart.omp.eu/Public/documentation/contenu/documentation/DART_User_Manual.pdf) for more details about DART-Lux simulation preparation.

Acknowledgements

This work is funded by Région Occitanie Pyrénées-Méditerranée, France and the TOSCA program of French Space Agency (CNES). We are also grateful for the support of DART team scientists (Dr N. Lauret, X. Yang, J. Guilleux, E. Chavanon).

Reference

Anderson, G.P., Clough, S.A., Kneizys, F.X., Chetwynd, J.H., Shettle, E.P., 1986. AFGL atmospheric constituent profiles (0.120 km). AIR FORCE GEOPHYSICS LAB HANSCOM AFB MA.

Berk, A., Anderson, G.P., Acharya, P.K., Shettle, E.P., 2008. MODTRAN5. 2.0. 0 user's manual. Spectr. Sci. Inc., Burlingt. MA, Air Force Res. Lab. Hanscom MA.

Berk, A., Bernstein, L.S., Robertson, D.C., 1987. MODTRAN: A moderate resolution model for LOWTRAN. SPECTRAL SCIENCES INC BURLINGTON MA.

Chavez Jr, P.S., 1988. An improved dark-object subtraction technique for atmospheric scattering correction of multispectral data. Remote Sens. Environ. 24, 459–479.

Conel, J.E., Green, R.O., Vane, G., Bruegge, C.J., Alley, R.E., Curtiss, B.J., 1987. AIS-2 radiometry and a comparison of methods for the recovery of ground reflectance.

Crippen, R.E., 1987. The regression intersection method of adjusting image data for band ratioing. Int. J. Remote Sens. 8, 137–155.

Dave, J. V, 1980. Effect of atmospheric conditions on remote sensing of a surface nonhomogeneity. Photogramm. Eng. Remote Sensing 46, 1173–1180.

Emde, C., Buras, R., Mayer, B., 2011. ALIS: An efficient method to compute high spectral resolution polarized solar radiances using the Monte Carlo approach. J. Quant. Spectrosc. Radiat. Transf. 112, 1622–1631.

Gastellu-Etchegorry, J.-P., Demarez, V., Pinel, V., Zagolski, F., 1996. Modeling radiative

transfer in heterogeneous 3-D vegetation canopies. Remote Sens. Environ. 58, 131–156.

Gastellu-Etchegorry, J.-P., Lauret, N., Yin, T., Landier, L., Kallel, A., Malenovský, Z., Al Bitar, A., Aval, J., Benhmida, S., Qi, J., 2017. DART: recent advances in remote sensing data modeling with atmosphere, polarization, and chlorophyll fluorescence. IEEE J. Sel. Top. Appl. Earth Obs. Remote Sens. 10, 2640–2649.

Goetz, A.F.H., Boardman, J.W., Kindel, B.C., Heidebrecht, K.B., 1997. Atmospheric corrections: on deriving surface reflectance from hyperspectral imagers, in: Imaging Spectrometry III. International Society for Optics and Photonics, pp. 14–22.

Grau, E., Gastellu-Etchegorry, J.-P., 2013. Radiative transfer modeling in the Earth–Atmosphere system with DART model. Remote Sens. Environ. 139, 149–170.

Guanter, L., Segl, K., Kaufmann, H., 2009. Simulation of optical remote-sensing scenes with application to the EnMAP hyperspectral mission. IEEE Trans. Geosci. Remote Sens. 47, 2340–2351.

Guillevic, P., Gastellu-Etchegorry, J.P., Demarty, J., Prévot, L., 2003. Thermal infrared radiative transfer within three-dimensional vegetation covers. J. Geophys. Res. Atmos. 108.

Guillevic, P.C., Bork-Unkelbach, A., Göttsche, F.M., Hulley, G., Gastellu-Etchegorry, J.-P., Olesen, F.S., Privette, J.L., 2013. Directional viewing effects on satellite land surface temperature products over sparse vegetation canopies—A multisensor analysis. IEEE Geosci. Remote Sens. Lett. 10, 1464–1468.

Kraska, T.A., 1996. DIRSIG: Digital Imaging and Remote Sensing Image Generation Model: Infrared Airborne Validation and Input Parameter Analysis. AIR FORCE INST OF TECH WRIGHT-PATTERSON AFB OH.

Myneni, R.B., Asrar, G., 1994. Atmospheric effects and spectral vegetation indices. Remote Sens. Environ. 47, 390–402.

Pharr, M., Jakob, W., Humphreys, G., 2016. Physically based rendering: From theory to implementation. Morgan Kaufmann.

Pinty, B., Gobron, N., Widlowski, J., Gerstl, S.A.W., Verstraete, M.M., Antunes, M., Bacour, C., Gascon, F., Gastellu, J., Goel, N., 2001. Radiation transfer model intercomparison (RAMI) exercise. J. Geophys. Res. Atmos. 106, 11937–11956.

Pinty, B., Widlowski, J., Taberner, M., Gobron, N., Verstraete, M.M., Disney, M., Gascon, F., Gastellu, J., Jiang, L., Kuusk, A., 2004. Radiation Transfer Model Intercomparison (RAMI) exercise: Results from the second phase. J. Geophys. Res. Atmos. 109.

Qi, J., Xie, D., Yin, T., Yan, G., Gastellu-Etchegorry, J.-P., Li, L., Zhang, W., Mu, X., Norford, L.K., 2019. LESS: LargE-Scale remote sensing data and image simulation framework over heterogeneous 3D scenes. Remote Sens. Environ. 221, 695–706.

Richtsmeier, S.C., Berk, A., Bernstein, L.S., Adler-Golden, S.M., 2001. A 3-Dimensional radiative-transfer hyperspectral image simulator for algorithm validation, in: International Symposium on Spectral Sensing Research. p. 15.

Shettle, E.P., Fenn, R.W., 1979. Models for the aerosols of the lower atmosphere and the effects of humidity variations on their optical properties. Optical Physics Division, Air Force Geophysics Laboratory.

Song, C., Woodcock, C.E., Seto, K.C., Lenney, M.P., Macomber, S.A., 2001. Classification and change detection using Landsat TM data: when and how to correct atmospheric effects? Remote Sens. Environ. 75, 230–244.

Ueno, S., Mukai, S., 1977. Atmospheric effects on remotely sensed data from space. IFAC Proc. Vol. 10, 423–428.

Veach, E., 1997. Robust Monte Carlo methods for light transport simulation. Stanford University PhD thesis.

Veach, E., Guibas, L., 1995a. Bidirectional estimators for light transport, in: Photorealistic

433 Rendering Techniques. Springer, pp. 145–167.
434 Veach, E., Guibas, L.J., 1995b. Optimally combining sampling techniques for Monte Carlo
435 rendering, in: Proceedings of the 22nd Annual Conference on Computer Graphics and
436 Interactive Techniques. pp. 419–428.
437 Verhoef, W., 1984. Light scattering by leaf layers with application to canopy reflectance
438 modeling: The SAIL model. Remote Sens. Environ. 16, 125–141.
439 Vermote, E.F., Tanré, D., Deuze, J.L., Herman, M., Morcette, J.-J., 1997. Second simulation of
440 the satellite signal in the solar spectrum, 6S: An overview. IEEE Trans. Geosci. Remote
441 Sens. 35, 675–686.
442 Wang, Y., Gastellu-Etchegorry, J.-P., 2020. DART: Improvement of thermal infrared radiative
443 transfer modelling for simulating top of atmosphere radiance. Remote Sens. Environ. 251,
444 112082.
445 Wang, Y., Lauret, N., Gastellu-Etchegorry, J.-P., 2020. DART radiative transfer modelling for
446 sloping landscapes. Remote Sens. Environ. https://doi.org/10.1016/j.rse.2020.111902
447 White, H.P., Khurshidt, K.S., Hitchcock, R., Neville, R., Sun, L., Champagne, C.M., Staenz,
448 K., 2004. From At-Sensor observation to At-Surface reflectance-calibration steps for earth
449 observation hyperspectral sensors, in: IGARSS 2004. 2004 IEEE International Geoscience
450 and Remote Sensing Symposium. IEEE, pp. 3241–3244.
451 Widlowski, J.-L., Mio, C., Disney, M., Adams, J., Andredakis, I., Atzberger, C., Brennan, J.,
452 Busetto, L., Chelle, M., Ceccherini, G., 2015. The fourth phase of the radiative transfer
453 model intercomparison (RAMI) exercise: Actual canopy scenarios and conformity testing.
454 Remote Sens. Environ. 169, 418–437.
455 Widlowski, J., Pinty, B., Lopatka, M., Atzberger, C., Buzica, D., Chelle, M., Disney, M.,
456 Gastellu-Etchegorry, J., Gerboles, M., Gobron, N., 2013. The fourth radiation transfer
457 model intercomparison (RAMI-IV): Proficiency testing of canopy reflectance models with

458 ISO-13528. J. Geophys. Res. Atmos. 118, 6869–6890.
459 Widlowski, J., Taberner, M., Pinty, B., Bruniquel-Pinel, V., Disney, M., Fernandes, R.,
460 Gastellu-Etchegorry, J., Gobron, N., Kuusk, A., Lavergne, T., 2007. Third Radiation
461 Transfer Model Intercomparison (RAMI) exercise: Documenting progress in canopy
462 reflectance models. J. Geophys. Res. Atmos. 112.
463 Yin, T., Gastellu-Etchegorry, J.-P., Lauret, N., Grau, E., Rubio, J., 2013. A new approach of
464 direction discretization and oversampling for 3D anisotropic radiative transfer modeling.
465 Remote Sens. Environ. 135, 213–223.
466 Zahidi, U., 2019. An End to End Hyperspectral Scene Simulator with Alternate Adjacency
467 Models and Its Comparison with CameoSim.
468 Wang Y., Kallel A., Yang X., Regaieg O., Lauret N., Guilleux J., Chavanon E., Gastellu-
469 Etchegorry J.P., DART-Lux: an unbiased and rapid Mont-Carlo radiative transfer method for
470 simulating remote sensing images (under preparation)